Full vectorial mapping of the complex electric near-fields of THz resonators

Arkabrata Bhattacharya and Jaime Gómez Rivas

Citation: APL Photonics **1**, 086103 (2016); doi: 10.1063/1.4962905
View online: http://dx.doi.org/10.1063/1.4962905
View Table of Contents: http://aip.scitation.org/toc/app/1/8
Published by the American Institute of Physics

Full vectorial mapping of the complex electric near-fields of THz resonators

Arkabrata Bhattacharya[1,2,a] and Jaime Gómez Rivas[1,3,b]
[1]*Dutch Institute for Fundamental Energy Research, DIFFER, P.O. Box 6336 5600 HH Eindhoven, The Netherlands*
[2]*FOM Institute AMOLF, P.O. Box 41883 1009 DB Amsterdam, The Netherlands*
[3]*Cobra Research Institute, Eindhoven University of Technology, Postbus 513, 5600 MB Den Dolech 2, 5612 AZ, The Netherlands*

(Received 14 April 2016; accepted 5 September 2016; published online 27 September 2016)

Using micro-structured photo-conducting probes, we demonstrate full vectorial mapping of the complex electric fields in the near-field region of a resonant structure at THz frequencies. The investigated structure represents the simplest case of a resonator: a metallic rod. We show field amplitude as well as phase maps for the three field components at the half wavelength ($\lambda/2$) resonance of the rod. The field as well as the phase distributions are in excellent agreement with our physical understanding of local electric-field distributions in the vicinity of $\lambda/2$ resonant structures and are validated by numerical simulations. These measurements can be a platform for performance optimization of the emerging field of THz photonic and plasmonic devices with complex sub-wavelength structures.
[http://dx.doi.org/10.1063/1.4962905]

I. INTRODUCTION

The angular spectral decomposition of an electromagnetic wave leads to two terms: a collection of propagating plane waves (far-field) and a distribution of spatially inhomogeneous non-propagating evanescent waves (near-field). At sub-wavelength distances from the source, the contribution due to the near-field is significant compared to the far-field. These distances are referred to as the near-field region.[1,2] The initial motivation to measure the near-field was an attempt to break the 'diffraction-limit' of far-field imaging. These studies led to the feasibility of accessing and probing directly the electromagnetic field formation near sub-wavelength structures. Advances in near-field microscopy opened the world of manipulation of light in sub-wavelength volumes leading to several promising applications in the field of photonics.[3–8] Attempts to measure and characterize near-fields were done first at optical frequencies, which paved the way for near-field detection techniques at THz frequencies.[9–20]

Owing to the relatively long wavelengths of THz radiation (~100's of microns), the creation of highly confined THz local fields in small volumes is critical for enhancing the interaction of THz waves with matter. The use of resonant structures for this purpose has been the topic of many interesting studies, especially for spectroscopy of deep-subwavelength structures.[21–28] For these studies, it is important that the vectorial electromagnetic fields around these resonant structures are fully characterized both in frequency and space to ensure optimal performance. This characterization becomes more relevant owing to the significant frequency shift between resonances measured in the far- and the near-field.[29,30] This shift has been recently shown to reach values comparable to the line-width of the resonance at THz frequencies due to the Fano interference in the far-field

[a]a.bhattacharya@differ.nl
[b]J.gomezrivas@differ.nl

between the incident and scattered fields.[31] Therefore, the sole characterization of the far-field is not sufficient to describe resonant THz structures.

In the past, several groups have shown vectorial mapping of in-plane electric near-fields in optical and infrared frequencies by scattering polarization resolved techniques.[32–35] These techniques offer a high spatial resolution but the detected field at different positions is a superposition of different field components.[36] Vectorial mapping of near electromagnetic fields at THz frequencies offers the potential to gather full information as local fields rather than intensity, which can be measured as a function of time. Several schemes have been developed for this purpose. Vectorial mapping of near-field components of resonant structures has been measured on top of non-linear crystals, using electro-optic detection.[37–39] This approach is limited by the necessity of having the sample on top of the high refractive index crystal and thus modifies the intrinsic near-field distribution of the investigated structure. Another approach uses electro-optic crystals as an external near-field probe.[40] This technique is limited by low sensitivity as well as partial invasiveness to the near-fields. Out-of-plane magnetic fields have been calculated from direct measurements of in-plane electric fields using photo-conductive (PC) antennas on substrates.[41,42] Direct measurement of magnetic fields in the near-field region has also been demonstrated.[43]

In this article, we use photoconductive switches imprinted on 1-μm-thin low-temperature-grown GaAs micro-probe tips[17] to measure all the individual components of the complex electric near-field in three dimensions near a gold rod resonant at THz frequencies. It has already been shown that these tips show negligible invasiveness to resonant structures.[31,44] Also, as the signal-to-noise ($\sim 10^4$ in intensity) and the rejection ratio for cross polarizations ($\sim 10^3$ in intensity) in our measurements are high, we can characterize both the spatial distributions of spectral intensity and phase of all the electric field components with high accuracy. These results are in very good agreement with the basic understanding of local field distributions at resonances and are further validated by numerical simulations.

II. EXPERIMENTAL TECHNIQUE

To demonstrate the spatial distribution of the near-field components of the electric field, we used the simplest sample geometry: a micro-rod resonant at THz frequencies. The sample consists of a rectangular rod made of gold on a quartz substrate. The dimensions of the rod are 100 μm along the long axis and 40 μm along the short axis. The height of the rod is 100 nm. The fabrication was done using UV lithography in combination with standard gold evaporation and subsequent lift-off techniques. A single rod was made on the substrate to avoid perturbation of the near-field due to the presence of other scatterers. The near-field micro-spectroscopy setup is driven by a femtosecond IR oscillator operating at 800 nm with a pulse duration of 20 fs and a repetition rate of 80 MHz. The output train of pulses from this oscillator is divided into two beams. The first beam which carries most of the power (~350 mW) goes through a delay stage and is incident on a photo-conductive (PC) antenna which generates broadband THz radiation.[45] This radiation is weakly focussed onto the sample position by a pair of off-axis parabolic mirrors. The other beam carries a small amount of power (~5 mW) and is used to bias the detector. This detector is a micro-probe-tip,[17] which operates on the principle of photo-conductive sampling.[46] The tip is a PC antenna downsized to sub-wavelength volumes (10 μm^2). The orientation of the PC gap in the tip defines the electric near-field component that it probes, as shown in Fig. 1 and explained later. The power rejection ratio of the microprobe for the other polarizations is more than 3 orders of magnitude. For each position in the delay stage of the first optical beam, which corresponds to a well defined temporal position in the THz electric field time-transient, the tip generates a proportional current. This current is amplified and measured using lock-in detection. By changing the delay of the THz pulse with respect to the bias probe-pulse, the whole THz transient can be measured and hence the transient electric field component of the near-field can be obtained.

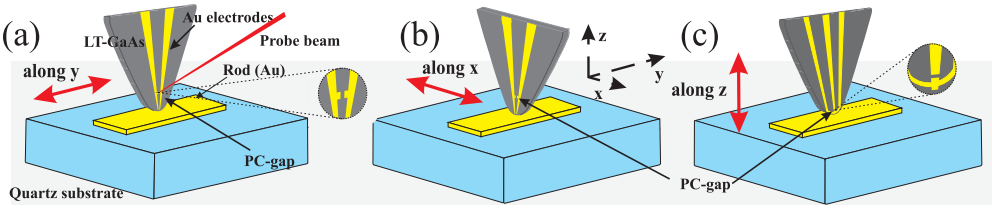

FIG. 1. Schematic representation of the probe-tips (TeraSpike TD-800-X-HR, Protemics GmbH) for measuring the different near-field components. (a) shows the PC-gap oriented along the long axis (Y) of the rod. Zoomed image of the PC gap is shown. (b) shows the same probe-tip oriented along the X axis, and (c) shows another probetip (TeraSpike TD-800-Z-N, Protemics GmbH) for measuring the Z-component of the near-field. The red arrows indicate the orientations of the PC-gaps in the probe-tips and hence the measured field component of the electric near field. The sample is illuminated by a broadband THz source from below. The THz polarization is along the long axis of the rod in all the cases, i.e., along Y-axis.

III. TERAHERTZ NEAR-FIELD IMAGING

The sample was mounted on a 3D configuration of linear translational stages enabling the probe-tip to measure the near-field at any position in the vicinity of the sample. All the near-field measurements were done on a plane with tip-to-sample distance of 1 μm. The polarization of the incident THz radiation was oriented along the Y axis. The long axis of the gold rod was also oriented with the Y-axis such that the length of the rod is parallel to the polarization of the THz beam. For measuring the in-plane (Y and X) field components of the electric field, we used the same probe-tip in parallel and crossed configurations as shown in Figs. 1(a) and 1(b). For measuring the out-of-plane (Z) component, we used a different probe-tip which has the PC gap oriented along the Z axis as shown in Fig. 1(c). Figure 2(a) shows the different components of the electric field transients measured by the probe-tips as a function of time delay at one of the corners of the gold rod. The field strength for the Y component (green open circles) is the highest as the incident field is along Y-axis. The X-component (blue open triangles) of the electric field in the

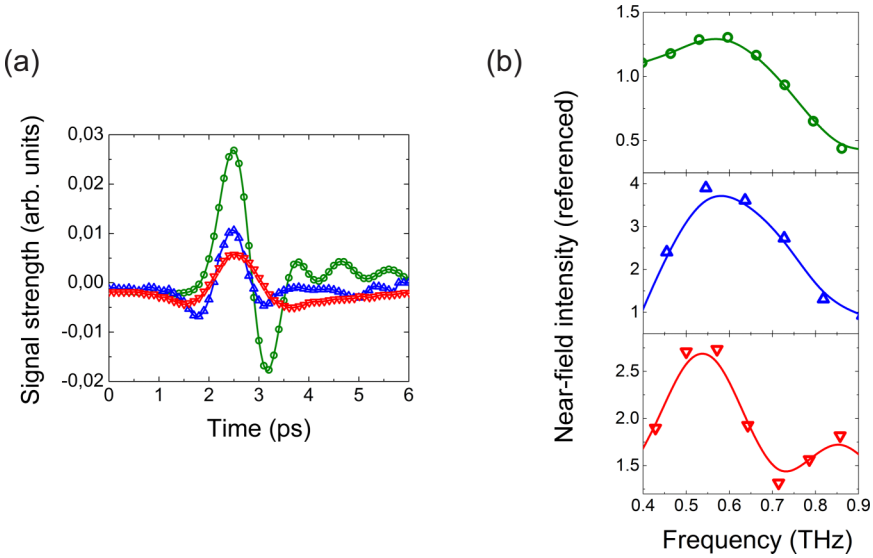

FIG. 2. (a) Transient response of each component of the electric near-field 1 μm above a corner of the Au rod when irradiated with broadband THz pulses. The green open circles show the Y-component (parallel to incident polarization) of the detected electric field. In blue open triangles is the X-component (crossed with the incident polarization) and in red open inverted triangles is the Z-component (out-of-plane). The X-field is multiplied by a factor of 5 and the Z-field by a factor of 10. Symbols indicate measured data, whereas the solid curves are guides to the eye. Panel (b) shows the spectral response of three different electric near-field components. The color schemes are same as in (a). The spectra have been referenced with the corresponding measurements from a bare substrate with the tip at the same height.

same figure is multiplied by a factor of 5 and the Z component (red open inverted triangles) by a factor of 10 to elucidate their temporal responses compared to the Y-component at the same position on the sample. Figure 2(b) shows the spectra derived from the transients of Fig. 2(a) by Fourier transformation and referencing to the corresponding bare substrate measurements. There is a clear resonant response at around 0.6 THz for all the field components. When the rod is illuminated by a broadband THz excitation, the charges near the surface of the rod are set into coherent oscillations. This forms a surface wave, which travels back and forth along the long axis of the rod (along Y). This oscillation of surface charges gives rise to a scattered field as well as an evanescent distribution of local fields around the rod. The local fields around the rods are highly enhanced near the sharp corners of the rod due to a large density of surface charges (lightning-rod effect). The frequency response of the surface charges is shaped by the geometry of the rod (also by the intrinsic losses) which gives rise to the resonant behavior at a well defined frequency. The local- or near-field intensity reaches its maximum at approximately the wavelength that corresponds to twice the dimension (l) of the rod which is oriented to the incident polarization. This is known as the $\lambda/2$ resonance as shown in Fig. 2(b). Higher order resonances in the response (not shown here) are also generated following the progression $l \approx n\lambda/2$, where n is the order of the resonance. It should be noted that the measured near-field intensities normalized by the reference measurement on a bare substrate shown in Fig. 2(b) do not represent the resonant local field enhancement. As the tip has a finite spatial resolution, the values of the electric field in the near-field measurements are averaged over a finite area. For the Y-component of the near-field, the tip also detects a fraction of the incident field that is not scattered by the rod. This intensity is also present in the reference measurement of the bare substrate and it is factorized by the normalization of the measurement. This non-resonant incident field is less relevant for the X- and Z-components of the electric field measurements due to the crossed polarization of these components with respect to the incident field. This explains the larger referenced near-field intensities for the X- and Z-components.

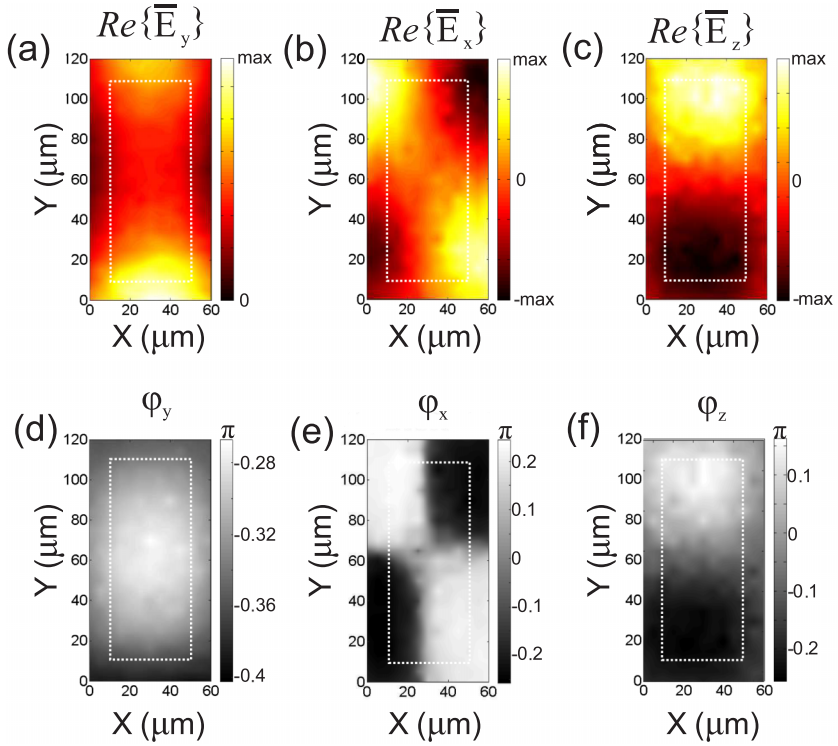

FIG. 3. (a), (b), and (c) show the spatial distribution of the real component of the different electric near-field components (Y, X, and Z, respectively) around the gold rod at the resonant frequency, i.e., 0.6 THz. Panels (d), (e), and (f) show the spatial distribution of phase at the resonant frequency around the gold rod. The dotted white rectangles indicate the boundaries of the gold-rod. All the measurements are referenced to their corresponding bare substrate measurements.

The physics behind the mechanism of the resonance can be best explained by the spectral analysis of the data. As the near field transients are measured at all the points around the rod at a fixed sample-to-probe distance, the data extracted are in the form of a 3D matrix with in-plane spatial coordinates along the two axis and temporal delay along the third axis. Fourier transform allows us to get two more data-matrices of the electric field amplitude and phase as a function of spatial coordinates and frequency. We have obtained the spatial maps of the field amplitude and the phase at the resonance frequency for the three electric field components. These maps are shown in Fig. 3, where panels (a) and (d) represent the measured amplitude and phase of the Y-component of the electric near-field at 0.6 THz. Panels (b) and (e) show the maps of the X-component and (c) and (f) are the near-field maps of the Z-component. The boundaries of the rod are marked in Fig. 3 by the white dashed rectangles.

To verify our results, we have simulated, using Finite difference in time domain (FDTD) method, the local fields in the vicinity of a rod. The rod has the same dimensions as explained earlier and it is illuminated by a broadband THz pulse similar to the experiments. Gold at THz frequencies behaves almost like a perfect electric conductor. Therefore, in our simulation we define

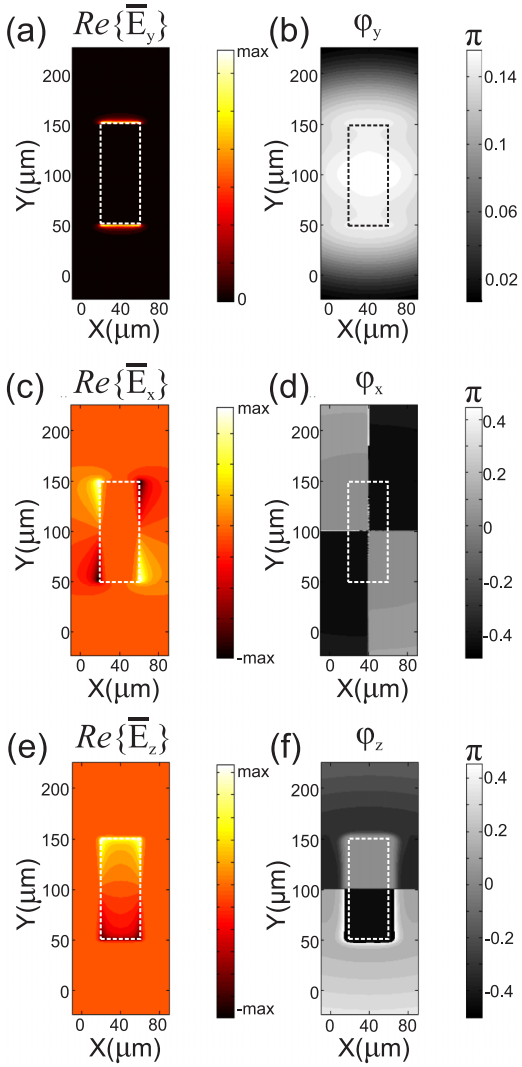

FIG. 4. (a), (c), and (e) show the spatial distribution of the simulated real component of the different electric near-field components (Y, X, and Z, respectively) around the perfect electric conductor rod at the resonant frequency. Panels (b), (d), and (f) show the spatial distribution of simulated phase at the resonant frequency around the rod. The dotted rectangles indicate the boundaries of the rod.

the material of the rod as a perfect electric conductor. The simulation volume, containing a single rod, has boundaries that are perfectly matched in impedance to the environment. Figure 4 shows the spatial distributions of amplitude ((a), (c), and (e)) and phase ((b), (d), and (f)) of the different components of the simulated electric field at the resonant frequency at a height of 1 μm above the rod. The simulated field profiles qualitatively match the measured profiles. However, the features seen in the simulated field distributions are much sharper. This discrepancy is due to the fact that in the simulations we used a field monitor which has an infinitesimal resolution (10 nm), whereas the micro-probe tips in the measurements have a finite resolution (~10 μm). Hence, as explained before, the measured fields are averaged over a larger sampling area, which results into a smeared out signal, i.e., the real field distributions are convolved with the spatial resolution of the tip.

To elucidate further the unique amplitude and phase distributions associated with the individual field components near the rod, we have simulated the same rods as before, however, this time illuminated by a monochromatic THz light. The frequency of this radiation was chosen to be precisely the resonance frequency of the rod. We define two electric field monitors: the first detects the field in the XY plane at a height of 1 μm above the rod, while the second detects the field in the YZ plane in the middle of the rod, i.e., X = 0. The rod is denoted by the green rectangle in the in-plane (XY) and by the green line in the out-of-plane (YZ) electric field maps. The white arrows represent the electric field vectors. The magnitude of the local field intensity is shown by the color scale. We define the two times, t_1 and t_2, which represents two phases of the incident field at which the incident field amplitude reaches the positive and negative maxima in adjacent half cycles of one oscillation. Figures 5(a) and 5(c) represent the in-plane and out-of-plane electric field distributions,

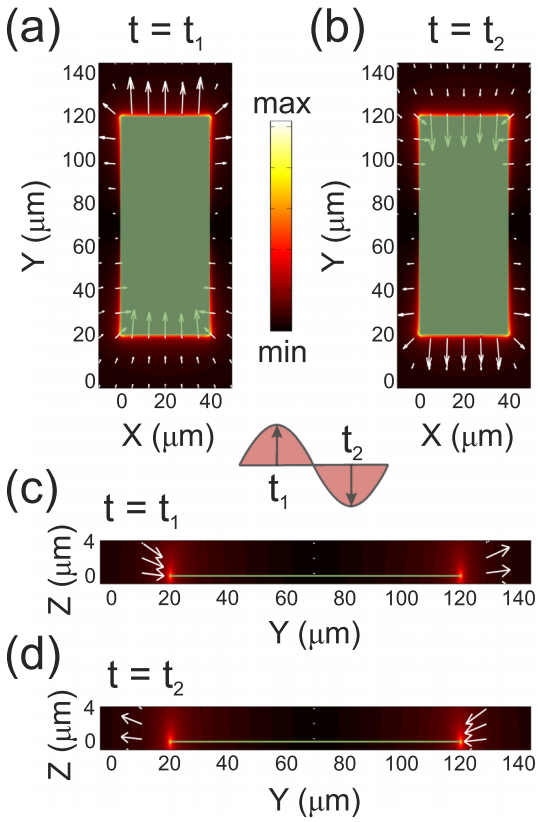

FIG. 5. Simulated electric field distribution near a gold rod (in green). The times t_1 and t_2 indicate the phase of the incident electric field at which the field amplitude reaches the positive and negative maxima, respectively. Panel (a) shows the in-plane electric field vectors (white arrows) thereby elucidating the in-plane field components, E_x and E_y, at $t = t_1$. Panel (b) shows the in-plane distribution of the electric field vectors at $t = t_2$. Panels (c) and (d) show the out-of-plane (cross-cut through the long axis of the rod) electric field vectors showing the E_y and E_z along the rod at $t = t_1$ and $t = t_2$, respectively. The color scale indicates the intensity of the local field in the maps.

respectively, in the vicinity of the rods at $t = t_1$. In Figs. 5(b) and 5(d) the same information is shown for $t = t_2$. If we project the electric field vectors in Figs. 5(a) and 5(b) along X and Y, it becomes evident that E_y at both the ends of the rod have equal magnitude and direction, which gets shifted by π radians in the next half cycle of the illuminating field. This explains the measured field distribution of Fig. 3(a). The uniform phase distribution of Fig. 3(d) is also described by the simulations because for all the edges of the rod E_y oscillates in-phase with the driving field. We see in Fig. 5(a) that the projection of the electric field vectors along X results in opposite orientation of E_x in the adjacent corners of the rod. This explains the formation of electric field 'hotspots' of opposite signs in the adjacent corners of the rod as shown in Fig. 3(b). E_x at the four corners of the rods oscillate with the driving field, but phase-shifted with respect to the adjacent corners, which gives rise to the phase distribution of E_x in Fig. 3(e). It is worth mentioning that along the long and the short axes of the rod, the magnitude of E_x goes to zero. The phase is not defined along these axes, which define lines of phase singularities. The phase singularity lines are clearly seen in the measurements of Fig. 3(e).

By analyzing Figs. 5(c) and 5(d), with similar reasoning, we can explain the field and phase distributions of E_z in Figs. 3(c) and 3(f). Again we see the formation of a phase singularity along the short axis of the rod. The field profiles in the measured maps in Fig. 3 are in excellent agreement with the explanation based on the simulated maps in Fig. 5.

IV. CONCLUSIONS

In conclusion, we have shown a complete characterization of near-fields generated near a resonator at THz frequencies. The field profiles were explained and supported by numerical simulations. The full vectorial characterization of the THz near-field will serve for the optimization of emerging photonic and plasmonic devices at THz frequencies.

ACKNOWLEDGMENTS

The authors thank Gopika Ramanandan, Alexei Halpin, Giorgos Georgiou, Michael Nagel, Simon Sawallich, and Christopher Matheisen for valuable discussions and for assistance with the experiments, Peter Govers for his help in the sample fabrication, and Niels Commandeur, Luc Blom, Jan Versluis, Duncan Verheijde, and Iliya Cerjak for technical support. We thank the financial support of ERC through Grant Nos. 259272 THZ-PLASMON (2010) and 665619 MicroMap (2014). We also thank the financial support of the Foundation for Fundamental Research on Matter (FOM), which is part of the Netherlands Organization for Scientific Research (NWO).

[1] J. Goodman, *Introduction to Fourier Optics* (McGraw-Hill, Roberts & Company, 2005).
[2] L. Novotny, in *The History of Near-Field Optics*, edited by E. Wolf, Progress in Optics Vol. 50 (Elsevier, 2007), Chap. V, pp. 137–184.
[3] J. R. Krenn, A. Dereux, J. C. Weeber, E. Bourillot, Y. Lacroute, J. P. Goudonnet, G. Schider, W. Gotschy, A. Leitner, F. R. Aussenegg, and C. Girard, Phys. Rev. Lett. **82**, 2590 (1999).
[4] H. Xu, J. Aizpurua, M. Käll, and P. Apell, Phys. Rev. E **62**, 4318 (2000).
[5] M. L. Brongersma, J. W. Hartman, and H. A. Atwater, Phys. Rev. B **62**, R16356 (2000).
[6] S. A. Maier, M. L. Brongersma, P. G. Kik, S. Meltzer, A. A. G. Requicha, and H. A. Atwater, Adv. Mater. **13**, 1501 (2001).
[7] N. N. Lepeshkin, A. Schweinsberg, G. Piredda, R. S. Bennink, and R. W. Boyd, Phys. Rev. Lett. **93**, 123902 (2004).
[8] F. Svedberg, Z. Li, H. Xu, and M. Käll, Nano Lett. **6**, 2639 (2006).
[9] S. Hunsche, M. Koch, I. Brener, and M. Nuss, Opt. Commun. **150**, 22 (1998).
[10] O. Mitrofanov, M. Lee, J. W. P. Hsu, I. Brener, R. Harel, J. F. Federici, J. D. Wynn, L. N. Pfeiffer, and K. W. West, IEEE J. Sel. Top. Quantum Electron. **7**, 600 (2001).
[11] K. Wang, D. M. Mittleman, N. C. J. van der Valk, and P. C. M. Planken, Appl. Phys. Lett. **85**, 2715 (2004).
[12] G. C. Cho, H.-T. Chen, S. Kraatz, N. Karpowicz, and R. Kersting, Semicond. Sci. Technol. **20**, S286 (2005).
[13] R. Lecaque, S. Grésillon, N. Barbey, R. Peretti, J.-C. Rivoal, and C. Boccara, Opt. Commun. **262**, 125 (2006).
[14] A. J. Huber, F. Keilmann, J. Wittborn, J. Aizpurua, and R. Hillenbrand, Nano Lett. **8**, 3766 (2008).
[15] A. J. Adam, J. M. Brok, P. C. Planken, M. A. Seo, and D. S. Kim, C. R. Phys. **9**, 161 (2008).
[16] A. Bitzer and M. Walther, Appl. Phys. Lett. **92**, 231101 (2008).
[17] M. Wächter, M. Nagel, and H. Kurz, Appl. Phys. Lett. **95**, 041112 (2009).
[18] F. Blanchard, A. Doi, T. Tanaka, H. Hirori, H. Tanaka, Y. Kadoya, and K. Tanaka, Opt. Express **19**, 8277 (2011).

[19] T. Cocker, J. Vedran, M. Gupta, S. Molesky, J. Burgess, G. Reyes, L. Titova, Y. Tsui, M. Freeman, and F. Hegmann, Nat. Photonics **7**, 620 (2013).
[20] O. Mitrofanov, F. Dominec, P. Kužel, J. L. Reno, I. Brener, U.-C. Chung, C. Elissalde, M. Maglione, and P. Mounaix, Opt. Express **22**, 23034 (2014).
[21] B. Ng, S. M. Hanham, V. Giannini, Z. C. Chen, M. Tang, Y. F. Liew, N. Klein, M. H. Hong, and S. A. Maier, Opt. Express **19**, 14653 (2011).
[22] A. Berrier, P. Albella, M. A. Poyli, R. Ulbricht, M. Bonn, J. Aizpurua, and J. G. Rivas, Opt. Express **20**, 5052 (2012).
[23] W. Withayachumnankul, H. Lin, K. Serita, C. M. Shah, S. Sriram, M. Bhaskaran, M. Tonouchi, C. Fumeaux, and D. Abbott, Opt. Express **20**, 3345 (2012).
[24] A. Berrier, M. C. Schaafsma, G. Nonglaton, J. Bergquist, and J. G. Rivas, Biomed. Opt. Express **3**, 2937 (2012).
[25] S. J. Park, J. T. Hong, S. J. Choi, H. S. Kim, W. K. Park, S. T. Han, J. Y. Park, S. Lee, D. S. Kim, and Y. H. Ahn, Sci. Rep. **4**, 4988 (2014).
[26] R. Singh, W. Cao, I. Al-Naib, L. Cong, W. Withayachumnankul, and W. Zhang, Appl. Phys. Lett. **105**, 171101 (2014).
[27] K. Ueno, S. Nozawa, and H. Misawa, Opt. Express **23**, 28584 (2015).
[28] S. R. J. Bhatt, P. Bhatt, P. Deshmukh, B. R. Sangala, M. N. Satyanarayan, G. Umesh, and S. S. Prabhu, J. Infrared, Millimeter, Terahertz Waves **37**, 795 (2016).
[29] N. Yu, P. Genevet, F. Aieta, M. A. Kats, R. Blanchard, G. Aoust, J. P. Tetienne, Z. Gaburro, and F. Capasso, IEEE J. Sel. Top. Quantum Electron. **19**, 4700423 (2013).
[30] P. Alonso-González, P. Albella, F. Neubrech, C. Huck, J. Chen, F. Golmar, F. Casanova, L. E. Hueso, A. Pucci, J. Aizpurua, and R. Hillenbrand, Phys. Rev. Lett. **110**, 203902 (2013).
[31] A. Bhattacharya, G. Georgiou, S. Sawallich, C. Matheisen, M. Nagel, and J. Gómez Rivas, Phys. Rev. B **93**, 035438 (2016).
[32] J. A. Veerman, A. M. Otter, L. Kuipers, and N. F. van Hulst, Appl. Phys. Lett. **72**, 3115 (1998).
[33] K. G. Lee, H. W. Kihm, J. E. Kihm, W. J. Choi, H. Kim, C. Ropers, D. J. Park, Y. C. Yoon, S. C. Choi, D. H. Woo, J. Kim, B. Lee, Q. H. Park, C. lienau, and D. S. Kim, Nat. Photonics **1**, 53 (2007).
[34] A. E. Klein, N. Janunts, M. Steinert, A. Tünnermann, and T. Pertsch, Nano Lett. **14**, 5010 (2014).
[35] P. Sarriugarte, M. Schnell, A. Chuvilin, and R. Hillenbrand, ACS Photonics **1**, 604 (2014).
[36] T. Neuman, P. Alonso-González, A. Garcia-Etxarri, M. Schnell, R. Hillenbrand, and J. Aizpurua, Laser Photonics Rev. **9**, 637 (2015).
[37] K. Yang, L. P. B. Katehi, and J. F. Whitaker, Appl. Phys. Lett. **77**, 486 (2000).
[38] M. A. Seo, A. J. L. Adam, J. H. Kang, J. W. Lee, S. C. Jeoung, Q. H. Park, P. C. M. Planken, and D. S. Kim, Opt. Express **15**, 11781 (2007).
[39] J. R. Knab, A. J. L. Adam, M. Nagel, E. Shaner, M. A. Seo, D. S. Kim, and P. C. M. Planken, Opt. Express **17**, 15072 (2009).
[40] D.-J. Lee, N.-W. Kang, J.-H. Choi, J. Kim, and J. F. Whitaker, Sensors **11**, 806 (2011).
[41] A. Bitzer, H. Merbold, A. Thoman, T. Feurer, H. Helm, and M. Walther, Opt. Express **17**, 3826 (2009).
[42] A. Bitzer, A. Ortner, and M. Walther, Appl. Opt. **49**, E1 (2010).
[43] N. Kumar, A. C. Strikwerda, K. Fan, X. Zhang, R. D. Averitt, P. C. M. Planken, and A. J. L. Adam, Opt. Express **20**, 11277 (2012).
[44] Y. Xu, X. Zhang, Z. Tian, J. Gu, C. Ouyang, Y. Li, J. Han, and W. Zhang, Appl. Phys. Lett. **107**, 021105 (2015).
[45] E. R. Brown, F. W. Smith, and K. A. McIntosh, J. Appl. Phys. **73**, 1480 (1993).
[46] J. Kim, S. Williamson, J. Nees, S. Wakana, and J. Whitaker, Appl. Phys. Lett. **62**, 2268 (1993).